Published in final edited form as:
IEEE Trans Med Imaging. 2010 February ; 29(2): 474–481. doi:10.1109/TMI.2009.2036843.

Imaging Electric Properties of Biological Tissues by RF Field Mapping in MRI

Xiaotong Zhang[1] **[Student Member, IEEE]**, **Shanan Zhu**[2], and **Bin He**[1,*] **[Fellow, IEEE]**
[1]Department of Biomedical Engineering, University of Minnesota, USA

[2]College of Electrical Engineering, Zhejiang University, China

Abstract

The electric properties (EPs) of biological tissue, i.e., the electric conductivity and permittivity, can provide important information in the diagnosis of various diseases. The EPs also play an important role in specific absorption rate (SAR) calculation, a major concern in high-field Magnetic Resonance Imaging (MRI), as well as in non-medical areas such as wireless-telecommunications. The high-field MRI system is accompanied by significant wave propagation effects, and the radio frequency (RF) radiation is dependent on the EPs of biological tissue. Based on the measurement of the active transverse magnetic component of the applied RF field (known as B_1-mapping technique), we propose a dual-excitation algorithm, which uses two sets of measured B_1 data to noninvasively reconstruct the electric properties of biological tissues. The Finite Element Method (FEM) was utilized in three-dimensional (3D) modeling and B_1 field calculation. A series of computer simulations were conducted to evaluate the feasibility and performance of the proposed method on a 3D head model within a transverse electromagnetic (TEM) coil and a birdcage (BC) coil. Using a TEM coil, when noise free, the reconstructed EP distribution of tissues in the brain has relative errors of 12% ~ 28% and correlated coefficients of greater than 0.91. Compared with other B_1-mapping based reconstruction algorithms, our approach provides superior performance without the need for iterative computations. The present simulation results suggest that good reconstruction of electric properties from B1 mapping can be achieved.

Index Terms

electric properties; B_1-mapping; Magnetic Resonance Electric Properties Tomography (MREPT); electrical impedance imaging

I. Introduction

The electric properties (EPs; conductivity σ and permittivity ε_r) of biological tissues at radio and microwave frequencies have been the subject of research for over four decades [1]. A comprehensive survey to date was conducted by Gabriel et al. [2-4], which covered a large selection of healthy tissue over a wide spectrum of frequencies (10Hz-20GHz). A few studies have also been conducted on EPs of a variety of cancerous tissue types at radio and microwave frequencies [5],[6],[7]. These studies have consistently shown that the EPs of cancerous tissues are three or more times greater than those of healthy tissue, and so it is anticipated that such EP information could be used in cancer detection. In addition, EPs are a determinant factor for the specific absorption rate (SAR), which is a major concern of

* Correspondence: Bin He. Ph.D., University of Minnesota, 7-105 NHH, 312 Church Street, SE, Minneapolis, MN 55455, USA, binhe@umn.edu.

safety in high-field Magnetic Resonance Imaging (MRI) systems and a critical problem in non-medical areas such as wireless-telecommunications.

In the past two decades, many efforts have been made to produce cross-sectional images of EPs *in vivo* by means of Electrical Impedance Tomography (EIT) [8-10] and its variants using magnetic induction (MIT) [11]. Both EIT and MIT are cost-effective and can provide dynamic information in regard to tissue EPs, but they are limited by low spatial resolution due to the surface measurements and the need to solve an ill-posed inverse problem. A technique called “Magnetic Resonance Electrical Impedance Tomography (MREIT)”, which is based on the Magnetic Resonance Current Density Imaging (MRCDI) technique [12] and measures current injection inducted MR phase shifts, has been pursued [13-16]. While MREIT eliminates the need to solve the ill-posed inverse problem and provides high spatial resolution in imaging electrical conductivity *in vivo*, it requires current injection into the body within an MRI scanner, which limits its applicability in medical applications. Another recently developed approach, Magnetoacoustic Tomography with Magnetic Induction (MAT-MI), offers the promise of obtaining high resolution tissue electrical conductivity profiles [17-20]. In MAT-MI, an object is placed in a static magnetic field and a pulsed magnetic field is applied to induce acoustic signals, which are then detected to reconstruct the tissue conductivity distribution. However, there have been no *in vivo* experiments reported so far.

Haacke et al. proposed a method of extracting EPs from MRI images [21]. They found that in 1.5T (and above) MRI systems, the wavelength of the radio frequency (RF) radiation was of the order of the body size, leading to a distortion of the RF field inside the irradiated object. By using an iterative sensitivity-matrix algorithm, these authors suggested that the EPs can be estimated using MRI images that reflect the disrupted RF profile. Wen later pointed out that the perturbation of the RF field in high-field MRI directly related to the conductivity and permittivity distribution within the sample, and a modified Helmholtz equation based non-iterative algorithm was proposed and tested in phantom experiments using 1.5T and 4.7T MRI [22]. Recently, using an iterative algorithm derived from Ampere's Law, Katscher et al. conducted an *in vivo* experiment using a 3T MRI system to image the EPs within a human head and leg [23], and named this approach “Magnetic Resonance Electric Properties Tomography (MREPT)”.

Signal intensity (SI) nonuniformity is distinct in high-field MRI systems. It can arise from a variety of factors, including imperfections in the scanner hardware and interactions between the magnetic field and biological tissues. Among these factors, electromagnetic (EM) interactions with the object have been shown to be the primary cause of SI nonuniformity for volume coils. It was reported that in 1.5T MRI systems, loaded birdcage (BC) coils had in-plane uniformity with 20% variation compared with as little as 1% variation when unloaded [24]. Through a series of experimental and simulation studies, it has been shown that the magnetic field distribution in the transverse plane of the coil is strongly dependent on the EPs of the biological tissues being studied [25]; moreover, the magnetic field distribution inside the RF coil at a high field can be studied and explained using Maxwell equations [26,27]. These findings have provided us with the mathematical framework to link EP distribution with MRI images.

The B_1-mapping technique [28-30] was developed to measure the rotating RF field components: the transmitted and received fields in RF coils. With the principle of reciprocity [31], the Cartesian transverse components of the RF magnetic field, H_x and H_y, can be derived. MREPT utilizes these two measurements to reconstruct the EP values within biological tissues, differing from other noninvasive imaging techniques in that no electrode mounting is required and no external energy is introduced into the body during MRI

scanning. It can be performed using a standard MRI system with a regular volume coil, and its spatial resolution is determined by MRI images and the quality of the applied B_1-mapping technique [23].

In the present study, a new non-iterative dual-excitation MREPT algorithm to image the tissue EPs is proposed, and the finite element method (FEM) [32] is utilized in RF coil modeling and B_1 field calculation. The performance of the proposed MREPT algorithm is evaluated using a five-tissue 3D anatomically accurate head model, a shielded 12-rung birdcage, and a transverse electromagnetic (TEM) coil.

II. Dual-excitation MREPT approach

A. Computation in high-frequency time-harmonic EM field – the forward problem

The RF field excited in MRI coils can be treated as a time-harmonic EM field [27]. Assuming the object of interest to be isotropic, and using the generalized Ampere circuit law and Faraday's magnetic induction law in a time-harmonic EM field, Helmholtz equation can be derived as [33]

$$\nabla \times [\mu_r^{-1} \cdot (\nabla \times \mathrm{E})] - \mathbf{k_0^2}\varepsilon_\mathbf{c} \cdot \mathrm{E} = -\mathbf{j}\omega\mu_\mathbf{0}\mathrm{J_s} \quad (1)$$

where **E** is the electric field vector, $\mathbf{J}_s$ the excitation current density in the coil, μ_0 the free space permeability, μ_r the relative permeability, ω the operating angular frequency, k_0 the vacuum wave number defined by $k_0=\omega\sqrt{\varepsilon_0\mu_0}$ with ε_0 as the free space permittivity, and ε_c the complex permittivity $\varepsilon_c = \varepsilon_r\varepsilon_0 - j\sigma/\omega$ with ε_r as the relative permittivity. Using the results of the electric field vector **E**, the magnetic field strength **H** can be obtained from [33]

$$\mathrm{H}=\mathbf{j}(\omega\mu_\mathbf{0}\mu_\mathbf{r})^{-\mathbf{1}} \cdot (\nabla \times \mathrm{E}) \quad (2)$$

The finite element method is normally used to solve electromagnetic problems, and with its flexibility in grid size, FEM can deal with objects having irregular geometries with good accuracy. In the present study, all EM fields were calculated through (1) and (2) by means of FEM using ANSYS 11.0 (ANSYS, Inc., PA, USA) software with its “high-frequency harmonic EM analysis”, whereas the postprocessing of EM field data was completed using MATLAB 2008a (The Mathworks Inc., Natick, MA).

The B_1-mapping technique measures rotating RF field components: the transmitted H_1^+ and received field H_1^- in RF coils. The principle of reciprocity [31] links magnetic field components in Cartesian and rotating frames via

$$\begin{cases} \mathrm{H}_1^+ = (H_x + jH_y)/2 \\ \mathrm{H}_1^- = (H_x - jH_y)^*/2 \end{cases} \quad (3)$$

where H_x and H_y are the x and y oriented RF magnetic fields created by the coil. We use (2) to derive these transverse magnetic components, and MREPT utilizes these two measurements to reconstruct the EP values of biological tissues.

B. Dual-excitation algorithm – the inverse problem

Consider the magnetic permeability inside biological tissues to be equal to that in a vacuum. Ampere's Law reads

$$\nabla \times \mathrm{H}=\sigma \mathrm{E}+\mathbf{j}\omega\varepsilon_{\mathbf{r}}\varepsilon_{\mathbf{0}}\mathrm{E} \quad (4)$$

Using the complex permittivity $\varepsilon_C = \varepsilon_r\varepsilon_0 - j\sigma/\omega$, we have

$$\nabla \times \mathrm{H}=\mathbf{j}\omega\varepsilon_{\mathbf{c}}\mathrm{E} \quad (5)$$

Taking the curl of both sides of (5) and substituting with $\nabla \times \mathbf{E} = -j\omega\mu_0\mathbf{H}$, we get

$$-\nabla^2\mathrm{H}=\omega^{\mathbf{2}}\mu_{\mathbf{0}}\varepsilon_{\mathbf{c}} \cdot \mathrm{H}+\mathbf{j}\omega(\nabla\varepsilon_{\mathbf{c}}) \times \mathrm{E} \quad (6)$$

or its matrix form

$$\begin{bmatrix} -\nabla^2 H_x \\ -\nabla^2 H_y \\ -\nabla^2 H_z \end{bmatrix} = \omega^2\mu_0\varepsilon_c \begin{bmatrix} H_x \\ H_y \\ H_z \end{bmatrix} + j\omega \begin{bmatrix} 0 & E_z & -E_y \\ -E_z & 0 & E_x \\ E_y & -E_x & 0 \end{bmatrix} \begin{bmatrix} \partial\varepsilon_c/\partial x \\ \partial\varepsilon_c/\partial y \\ \partial\varepsilon_c/\partial z \end{bmatrix} \quad (7)$$

According to Ampere's Law, we replace the electric field components with magnetic field components as follows

$$\begin{cases} E_x=(\partial H_z/\partial y - \partial H_y/\partial z)/j\omega\varepsilon_c \\ E_y=(\partial H_x/\partial z - \partial H_z/\partial x)/j\omega\varepsilon_c \\ E_z=(\partial H_y/\partial x - \partial H_x/\partial y)/j\omega\varepsilon_c \end{cases} \quad (8)$$

For regular birdcage coils, the axial z component of the end-ring generated magnetic field (H_z) is nonproductive for NMR excitation, and can become a source of ohmic loss to induced conduction currents in the tissue load conductor. To solve this problem, the TEM resonator was developed [34], in which the coil's return path follows the shield rather than the end rings, and a rung-current-generated transverse magnetic field without the counterproductive end-ring currents is achieved. In this case, we can neglect the H_z component in (8), and rewrite (7) as

$$\begin{cases} -\nabla^2 H_x = \omega^2\mu_0 H_x\varepsilon_c - (\partial H_x/\partial z)[(\partial\varepsilon_c/\partial z)/\varepsilon_c] \\ \qquad\qquad +(\partial H_y/\partial x - \partial H_x/\partial y)[(\partial\varepsilon_c/\partial y)/\varepsilon_c] \\ -\nabla^2 H_y = \omega^2\mu_0 H_y\varepsilon_c - (\partial H_y/\partial z)[(\partial\varepsilon_c/\partial z)/\varepsilon_c] \\ \qquad\qquad +(\partial H_y/\partial x - \partial H_x/\partial y)[(\partial\varepsilon_c/\partial x)/\varepsilon_c] \end{cases} \quad (9)$$

In (9), H_x and H_y distributions correspond to B_1-mapping results, while ε_c, $(\partial\varepsilon_c/\partial x)/\varepsilon_c$, $(\partial\varepsilon_c/\partial y)/\varepsilon_c$ and $(\partial\varepsilon_c/\partial z)/\varepsilon_c$ are unknown. Upon acquiring another set of $H_x \sim H_y$ data, we can form a set of linear equations with four equations and four unknown variables, and thus ε_c can be solved.

Two methods can be adopted to acquire two sets of $H_x \sim H_y$ data: (a) adjusting the RF coil excitation modes, such as linear (vertical and/or horizontal polarization) and/or quadrature modes [35], to excite the imaging object twice, separately, but with the same subject orientation; or (b) rotating the subject along the z-axis by an angle. In the present study, we used the linear excitation mode to generate two polarizations by switching the current feed points to positions 90 degrees apart from each other.

III. Materials and Methods

A. FEM Model of the Head and Coil

T1-weighted MRI images (128×128×72, 2×2×2mm^3) of a human head, which covered the entire brain, were acquired from a 3T Siemens MRI system. The head images were then segmented into five tissues: scalp, skull, CSF, WM and GM. The structural information was imported into ANSYS software, and a five-tissue anatomically accurate head model was constructed using a hexahedral element with a mesh size of 2×2×2mm^3, which is equivalent to the voxel size of MRI images.

A 12-rung birdcage coil and a TEM coil with diameters of 28cm and lengths of 28cm were modeled. Either coil was enclosed by a cylindrical shield having a diameter of 32cm and a length of 30cm. Both the coils and the shield(s) were meshed with the tetrahedral element and assigned with copper material. Fig. 1 illustrates the FEM models of the head and shielded birdcage coil in ANSYS, and Fig. 2 shows the structural views on the axial, sagittal and coronal planes.

Since all RF coils are basically open structures, the field generated by a coil radiates into a large space. However, a numerical simulation can be performed only inside a finite space. Therefore, we must first truncate the simulation space by using an air volume to enclose the solution area. In order to reduce the artificial field reflection produced by the volume, we used a Perfectly Matched Layer (PML) [36] to surround the artificial surface of the air volume. For our shielded coils, the shield provided the truncation at which the boundary condition $\hat{n} \times \mathbf{E} = 0$ should be applied [35]. Both air and PML volumes were discretized with the tetrahedral element.

B. Coil Excitation

To perform a linear excitation, the equivalent circuit model [35] was utilized to calculate the electric current in each rung. All of the capacitors in the coil were replaced with current sources at the required resonant frequency. For the birdcage coil, the current I_i^{rung} flowing in the ith rung is

$$I_i^{rung} = I_0 \sin[(i - 0.5)\pi/6] \quad (10)$$

where I_0 denotes the maximum current. In our study, I_0 was assumed to be unit current, so the current flowing in the end-rings between the ith and (i+1)th rungs is

$$I_i^{end-ring} = \pm \cos(i \cdot \pi/6)/0.52 \quad (11)$$

For the TEM coil, the current in each end-ring was assigned to be zero. Similar current configurations can also be found in [37].

$\pi/2$ and $\pi/6$ offset was added on the phase of the current flowing in the coil, separately, to simulate the current feed point switching. Three coil excitation schemes are listed in TABLE I.

C. Simulation Protocols

Simulations were conducted in 3T (128MHz) environment. The corresponding target EP values for different head tissues were derived from the 4-Cole-Cole Model [4] and are listed in Table II.

Using ANSYS software as the forward solver, we generated the simulated data of H_x and H_y by different coil excitation schemes, correspondingly. Simulations were conducted on both the birdcage coil and TEM coil to evaluate the influence of neglecting the H_z component in (9).

We define relative error (RE) and correlation coefficient (CC) of the reconstructed EPs images as

$$\begin{aligned} \mathrm{RE}_{\sigma_{tissue}} &= \sqrt{\sum_{i=1}^{N}(\sigma_i^* - \sigma_{tissue})^2/\sigma_{tissue}^2} \\ \mathrm{RE}_{\varepsilon_{tissue}} &= \sqrt{\sum_{i=1}^{N}(\varepsilon_i^* - \varepsilon_{tissue})^2/\varepsilon_{tissue}^2} \\ \mathrm{CC}_{\sigma_{tissue}} &= \sum_{i=1}^{N}(\sigma_i^* \cdot \sigma_{tissue})/\sqrt{N(\sigma_{tissue})^2 \cdot \sum_{i=1}^{N}(\sigma_i^*)^2} \\ \mathrm{CC}_{\varepsilon_{tissue}} &= \sum_{i=1}^{N}(\varepsilon_i^* \cdot \varepsilon_{tissue})/\sqrt{N(\varepsilon_{tissue})^2 \cdot \sum_{i=1}^{N}(\varepsilon_i^*)^2} \end{aligned} \quad (12)$$

where σ_{tissue} and ε_{tissue} are the target EP values, and σ_i^* and ε_i^* are the estimated values in the ith pixels within the specified tissue.

In order to test the noise tolerance of the proposed algorithm, we added Gaussian white noise (GWN) to the simulated B_1 field data. From (3) we get the circularly-polarized components of the B_1 field, then add GWN to the amplitude and phase of H_1^+ and H_1^-, respectively. The noise level is evaluated by SNR_{B1}, which is defined as follows

$$\mathrm{SNR}_{\mathrm{B1}} = A/s_{amp} \quad (13)$$

where A is the amplitude of the noise-free B_1 field voxel signal and s_{amp} is the standard deviation (STD) of amplitude noise. In the present study, we assumed SNR_{B1}=200, 150 and 100. Note that here, SNR_{B1} is different from the commonly denoted SNR of MRI systems (SNR_{MRI}). A related description can be found in the Discussion and Appendix.

The Wiener adaptive lowpass-filter was applied to pre-process the "contaminated" B_1 maps, and (3) was re-used to derive the H_x and H_y components.

IV. Simulation Results

We chose the central slice (z=0) of the head model as the slice of interest, and the corresponding MRI T1-weighted image is depicted in Fig. 3 (a). Figs. 3 (b1) and (c1) draw the target EP distributions after image segmentation. Using the 28cm-long TEM coil, with $H_x^1 \sim H_y^1$ and $H_x^1 \sim H_y^2$ data acquired from coil excitation schemes S1 and S2, the reconstructed EP distributions are shown in (b2) and (c2). Two bright stripe-like artifacts along the x- and y-axes are observed in above results, and this phenomenon resulted from the characteristics of the E_z distribution inside the linearly polarized RF coil. Figs. 4 (a) and (b) depict the modulus of the E_z distribution on the central axial slice within the head using S1 and S2 excitations, in which the E_z modulus varied rapidly and dropped to zero in the area across the x-axis in (a) and the y-axis in (b). We define $D_H = (\partial H_y/\partial x - \partial H_x/\partial y)$, and D_H has the same modulus distribution with E_z according to (8). Since D_H acts as a denominator in our algorithm as (9) indicates, its "zero" area would introduce numerical

errors, which are observed in the reconstruction results in Fig. 3 as two bright stripe-like artifacts.

To solve the above problem, we produced two new sets of $H_x^* \sim H_y^*$ data by

$$\begin{cases} H_x^{1*}=(H_x^1+jH_x^2)/2 \\ H_y^{1*}=(H_y^1+jH_y^2)/2 \end{cases} \text{ and } \begin{cases} H_x^{2*}=(H_x^1-jH_x^2)/2 \\ H_y^{2*}=(H_y^1-jH_y^2)/2 \end{cases} \quad (14)$$

In a linear medium, the system described by Maxwell's equations is a linear system; according to the superposition principle, H_x^* and H_y^* still hold for (9). Figs. 4 (c) and (d) show the $\|E_Z\|$ distribution corresponding to the new $H_x^* \sim H_y^*$ data, and Figs. 3 (b3) and (c3) show the reconstructed EP results using $H_x^* \sim H_y^*$ data when noise-free. The bright stripe-like artifacts disappear in the reconstructed images; however, there are still little artifacts in the reconstructed images, and they mainly resulted from much lower intensity of the $\|E_Z\|$ distribution in the central area, as Figs. 4 (c) and (d) depict, which is about 1/100 of the periphery intensity. Reconstruction results for CSF, WM and GM tissues are listed in TABLE III, and their relative errors range within 12% ~ 28% while correlated coefficients all above 0.91. Similar $H_x^* \sim H_y^*$ data processing have been applied in the following simulations.

In our algorithm, $\partial H_Z/\partial y$ and $\partial H_Z/\partial x$ are assumed to be negligible. Since birdcage coils have been widely used in clinical applications, it is necessary to evaluate the H_Z effects for regular birdcage coils. We applied the dual-excitation algorithm on the 28cm-long birdcage, and we also took $\partial H_Z/\partial y$ and $\partial H_Z/\partial x$ into equation (9) to finish the reconstruction using the same coil. In addition, we constructed a 12cm-long birdcage coil (with the same other geometrical parameters and configurations as the 28cm-long birdcage coil) to evaluate its performance. Coil excitation schemes S1 and S2 were applied. Reconstructed EPs distribution and simulation results are shown and summarized in Fig. 5 and TABLE III, respectively. It can be observed that, when H_Z component was considered we could surely improve EPs reconstruction results. However, while the experimental measurement of H_Z component is not feasible in MRI, it is also reasonable to assume $H_Z = 0$ within a common birdcage coil which could also provide well-differentiated structural information of biological tissues.

Fig. 6 shows the reconstructed EPs distribution when noise was added with SNR_{B1}=200, 150 and 100. The corresponding REs and CCs are summarized in TABLE IV. The 28cm-long TEM coil and S1 and S2 coil excitations were used. We also applied S2 and S3, S1 and S3 -- choosing two adjacent rungs as current feed points individually -- to excite the TEM coil with noise (SNR_{B1}=200). A comparison of the reconstruction results is depicted in Fig. 7. It can be observed that, when added with noise, all the tissues could be differentiated in the reconstruction results; and similar tissue patterns could also be produced while different coil excitation scheme combinations were utilized.

We also applied Wen's method in [22] to the TEM model by S1 and S2 excitations to reconstruct the EPs distribution. Fig. 8 shows the comparison of the reconstruction results when noise-free. It can be seen that we obtained better results around the tissue boundary regions, and this is because the term of $j\omega(\nabla \varepsilon_C) \times \mathbf{E}$ of (6) was not taken into account in the modified Helmholtz equation in Wen's method.

V. Discussion

Since the conductivity and permittivity values of tissues change with their physiological and pathological conditions, EP maps could provide useful diagnostic information. MREPT promises to reconstruct not only the conductivity distribution, as EIT, MIT, MREIT and MAT-MI aim to do, but also the permittivity distribution within biological tissues, thus enriching our observations of their conditions. In addition, as it is based on B_1-mapping, which has been developed and pursued for decades, MREPT does not require electrode mounting or external energy deposition, which pose potential safety concerns. It could provide a high spatial resolution in imaging EPs with the aid of MRI. In the present study, we have proposed a new dual-excitation MREPT algorithm, and as our simulation results indicate, the dual-excitation algorithm furnishes us with a practical approach to reconstructing the conductivity and permittivity distributions within a human head while avoiding the need to solve the ill-posed inverse problem present in traditional EIT. The desirable reconstruction results of tissues with heavier implications in physiology and pathology (such as CSF, WM and GM) suggest that MREPT imaging deserves further investigation, can be extended to other organs of the human body, and may have wide clinical applications.

In our algorithm, the z component of the magnetic field intensity H_z is neglected. Our simulation results suggest that the dual-excitation algorithm still works well, even using a typical birdcage coils (Fig. 5) in which the H_z component prominently exists and is mainly generated by end-rings. Using a TEM coil, we can get better reconstruction EP images with higher accuracy.

To eliminate the bright stripe-like artifacts in Fig. 2, we produced two new sets of $H_x^* \sim H_y^*$ according to the superposition principle. Alternatively, to generate a similar $\|E_z\|$ distribution as in Figs. 3 (c) and (d), we may also excite the coil by quadrature polarization which is commonly utilized in commercial RF coils. However, since our algorithm needs to excite the coil twice, at least three current feed points will be required to perform the quadrature excitation twice. Therefore, our approach of using data acquired from two linear excitations appears to be more feasible and easy to implement.

In contrast to the previously proposed MREPT algorithms in [21] and [23], our approach does not require iterative computation which needs precise coil and subject modeling and is time consuming. Compared with the method in [22], ours is more capable to deal with regions where the EPs distribute inhomogeneously and discontinuously. Fig. 8 illustrates this point.

Uniqueness of solution is an important issue in inverse problems. We applied three coil excitation schemes, and conducted the reconstruction procedures by choosing two 30°-apart (adjacent), 60°-apart and 90°-apart current feed points. It is shown in Fig. 7 that, under either excitation combination with noise added, our algorithm works well and produces overall similar distributions of the EPs. While these results suggest robustness and potential uniqueness characteristic of our algorithm, it is also indicated that when the switching current feed point is infeasible, our algorithm is still effective by careful subject rotation over a small angle inside the coil. In the future, the theoretical study on the uniqueness of the MREPT problem remains to be further performed.

In previous B_1 field simulation studies, the EP values were preset according to experimentally measured data [39] or the published 4-Cole-Cole dispersion relation [3]. However, in many instances, these two data are not in good agreement. Our algorithm will provide another effective way to accurately predict the EP values of biological tissues, and

will also substantially benefit future studies in the MRI domain as well as other areas that involve EP configuration in the range of radio frequency.

For isotropic biological tissues, the SAR is defined by

$$\mathrm{SAR}=\sigma(E_x^2+E_y^2+E_z^2)/2\rho \quad (15)$$

where ρ is the tissue density and is determined through experimental measurement. Once we get the B_1 distribution, the EP values can be obtained from the dual-excitation algorithm. Since H_x and H_y are more dominant in a birdcage and TEM coil, the electric field can be determined by Ampere's Law without H_z component, and we can directly calculate the SAR distribution. Thus, the evaluation of heat effects becomes more convenient.

In our algorithm, the Laplacian operation $\nabla^2\mathbf{H}$ amplifies noise effect. Thus the present algorithm is relatively sensitive to noise, as shown in Table IV when SNR drops. We have applied Wiener filtering over B_1 images; in addition, other feasible ways can be used to reduce noise level in experiment, such as taking multi-MRI scans in experiments and average B_1 images. Furthermore, for common B_1 mapping techniques, the scanning parameters are usually chosen as TR ≫ T1 ≫ TE, and the MRI image signal intensity depends on $\|\mathrm{H}_1^+\|$ and $\|\mathrm{H}_1^-\|$ via [21, 23, 38]

$$\mathrm{SI} \propto M_0 \cdot \sin(\gamma\|\mathrm{H}_1^+\|\tau)\|\mathrm{H}_1^-\| \quad (16)$$

where M_0 is the equilibrium magnetization, γ the gyromagnetic ratio of ^{1}H, and τ the duration of rectangular RF pulse. For small flip angle pulse, (16) can be written as

$$\mathrm{SI} \propto \gamma \cdot \tau \cdot M_0(\|\mathrm{H}_1^+\| \cdot \|\mathrm{H}_1^-\|) \quad (17)$$

and image signal intensity is propositional to $\|\mathrm{H}_1^+\| \cdot \|\mathrm{H}_1^-\|$. When we add noise into $\|\mathrm{H}_1^+\|$ and $\|\mathrm{H}_1^-\|$ leveled by SNR_{B1}, it can be proved that the corresponding SNR_{MRI} will be lower than SNR_{B1} (see Appendix); in other words, SNR_{B1} is $\sqrt{2}$ times higher than SNR_{MRI}. Moreover, note that we only consider noise in the B_1 field in such a case; since there are other noise sources in the MRI signal detection process, such as thermal fluctuation and electronics factors, SNR_{B1} is even higher than SNR_{MRI}. Therefore, our assumption that SNR_{B1} equals to 100 ~ 200 is reasonable for regular MRI scanning.

A multi-port quadrature coil can be driven at each one point by well-controlled RF drive circuit [34], thus it is applicable to acquire different B_1 data to finish the reconstruction. Besides, our algorithm requires B_1 field measurements. Until now, many B_1-mapping techniques have been proposed, and the measurement of B_1 field intensity has been well established, while phase measurement has been studied by few groups [22, 23, 40]. Recently, a novel B_1 phase mapping method was developed in local B_1 shimming studies for transceiver arrays [41], and it provides us with the possibility for accurate B_1 phase mapping. In the future, more efforts should be focused on the pursuit of B_1 complex image mapping in order to improve the efficiency and accuracy of the MREPT technique.

Acknowledgments

We would like to thank Drs. Yiping Du, Zhongmin Liu, Ulrich Katscher, Mr. Xu Li, and Ms. Yang Liu for useful discussions, and Mr. Won Hee Lee for technical assistance in the head FEM modeling. This work was supported in part by NIH R21EB006070, the NNSF of China (50577055), NSF BES-0602957, NIH R01EB007920, and the

Supercomputing Institute of the University of Minnesota. X.T. Zhang was partly supported by the Lu's Postgraduate Education International Exchange Fund of Zhejiang University.

Appendix: Derivation of SNRMRI From SNRB1

Noise in B1 field is leveled by $\mathrm{SNR}_{\mathrm{B1}}$ in (13) via

$$\mathrm{SNR}_{\mathrm{B1}} = \begin{cases} \|H_1^+\|/s_1 \\ \|H_1^-\|/s_2 \end{cases} \quad (18)$$

where $\|\mathrm{H}_1^+\|$ and $\|\mathrm{H}_1^-\|$ are noise-free voxel intensity, and s_1 and s_2 are the STD of two uncorrelated GWN added into $\|\mathrm{H}_1^+\|$ and $\|\mathrm{H}_1^-\|$, respectively. We use n_1 and n_2 to represent these two noise values. Then we have

$$(\|H_1^+\|+n_1)\cdot(\|H_1^-\|+n_2)=\|H_1^+\|\cdot\|H_1^-\|+\|H_1^+\|\cdot n_2+\|H_1^-\|\cdot n_1+n_1\cdot n_2 \quad (19)$$

with the variance as

$$\begin{aligned} &\mathrm{var}(\|H_1^+\|\cdot\|H_1^-\|+\|H_1^+\|\cdot n_2+\|H_1^-\|\cdot n_1+n_1\cdot n_2) \\ &=\|H_1^+\|^2\cdot\mathrm{var}(n_2)+\|H_1^-\|^2\cdot\mathrm{var}(n_1)+\mathrm{var}(n_1)\cdot\mathrm{var}(n_2) \\ &=s_2{}^2\cdot\|H_1^+\|^2+s_1{}^2\cdot\|H_1^-\|^2+s_1{}^2\cdot s_2{}^2 \\ &=\|H_1^+\|^2\cdot\|H_1^-\|^2(1/\mathrm{SNR}_{\mathrm{B1}}{}^2+1/\mathrm{SNR}_{\mathrm{B1}}{}^2+1/\mathrm{SNR}_{\mathrm{B1}}{}^4) \\ &\approx 2\|H_1^+\|^2\cdot\|H_1^-\|^2/\mathrm{SNR}_{\mathrm{B1}}{}^2 \end{aligned} \quad (20)$$

and the corresponding $\mathrm{SNR}_{\mathrm{MRI}}$ can be derived from (17) and (20) by

$$\begin{aligned} \mathrm{SNR}_{\mathrm{MRI}} &= \mathrm{SI}/\mathrm{STD}(\mathrm{SI}) \\ &=(\|H_1^+\|\cdot\|H_1^-\|)/(\sqrt{2}\|H_1^+\|\cdot\|H_1^-\|/\mathrm{SNR}_{\mathrm{B1}}) \\ &=\mathrm{SNR}_{\mathrm{B1}}/\sqrt{2} \end{aligned} \quad (21)$$

References

1. Fear EC, Li X, Hagness SC, Stuchly MA. Confocal microwave imaging for breast cancer detection: localization of tumors in three dimensions. IEEE Trans Biomed Eng. Aug; 2002 49(8):812–22. [PubMed: 12148820]
2. Gabriel C, Gabriel S, Corthout E. The dielectric properties of biological tissues .1. Literature survey. Phys Med Biol. Nov; 1996 41(11):2231–2249. [PubMed: 8938024]
3. Gabriel S, Lau RW, Gabriel C. The dielectric properties of biological tissues: II. Measurements in the frequency range 10 Hz to 20 GHz. Phys Med Biol. Nov; 1996 41(11):2251–69. [PubMed: 8938025]
4. Gabriel S, Lau RW, Gabriel C. The dielectric properties of biological tissues: III. Parametric models for the dielectric spectrum of tissues. Phys Med Biol. Nov; 1996 41(11):2271–93. [PubMed: 8938026]
5. Chaudhary SS, Mishra RK, Swarup A, Thomas JM. Dielectric properties of normal & malignant human breast tissues at radiowave & microwave frequencies. Indian J Biochem Biophys. Feb; 1984 21(1):76–9. [PubMed: 6490065]
6. Surowiec AJ, Stuchly SS, Barr JB, Swarup A. Dielectric properties of breast carcinoma and the surrounding tissues. IEEE Trans Biomed Eng. Apr; 1988 35(4):257–63. [PubMed: 2834285]

7. Joines WT, Zhang Y, Li C, Jirtle RL. The measured electrical properties of normal and malignant human tissues from 50 to 900 MHz. Med Phys. Apr; 1994 21(4):547–50. [PubMed: 8058021]
8. Kerner TE, Paulsen KD, Hartov A, Soho SK, Poplack SP. Electrical impedance spectroscopy of the breast: clinical imaging results in 26 subjects. IEEE Trans Med Imaging. Jun; 2002 21(6):638–45. [PubMed: 12166860]
9. Malich A, Bohm T, Facius M, Freessmeyer M, Fleck M, Anderson R, Kaiser WA. Additional value of electrical impedance scanning: experience of 240 histologically-proven breast lesions. Eur J Cancer. Dec; 2001 37(18):2324–30. [PubMed: 11720824]
10. Metherall P, Barber DC, Smallwood RH, Brown BH. Three-dimensional electrical impedance tomography. Nature. Apr 11; 1996 380(6574):509–12. [PubMed: 8606768]
11. Griffiths H, Stewart WR, Gough W. Magnetic induction tomography. A measuring system for biological tissues. Ann N Y Acad Sci. Apr 20.1999 873:335–45. [PubMed: 10372181]
12. Joy M, Scott G, Henkelman M. In vivo detection of applied electric currents by magnetic resonance imaging. Magn Reson Imaging. 1989; 7(1):89–94. [PubMed: 2918822]
13. Zhang, N. MS Thesis. Dept of Elec Eng., Univ Toronto; Toronto, ON, Canada: 1992. Electrical impedance tomography based on current density imaging.
14. Khang HS, Lee BI, Oh SH, Woo EJ, Lee SY, Cho MY, Kwon O, Yoon JR, Seo JK. J-substitution algorithm in Magnetic Resonance Electrical Impedance Tomography (MREIT): Phantom experiments for static resistivity images. IEEE Trans Med Imaging. Jun; 2002 21(6):695–702. [PubMed: 12166867]
15. Ider YZ, Onart S. Algebraic reconstruction for 3D magnetic resonance-electrical impedance tomography (MREIT) using one component of magnetic flux density. Physiol Meas. Feb; 2004 25(1):281–294. [PubMed: 15005322]
16. Zhang XT, Yan DD, Zhu SA, He B. Noninvasive Imaging of Head-Brain Conductivity Profiles. IEEE Eng Med Biol Mag. 2008; 27(5):78–83. [PubMed: 18799394]
17. Xu Y, He B. Magnetoacoustic tomography with magnetic induction (MAT-MI). Phys Med Biol. 2005; 50:5175–5187. [PubMed: 16237248]
18. Li X, Xu Y, He B. Imaging Electrical Impedance From Acoustic Measurements by Means of Magnetoacoustic Tomography With Magnetic Induction (MAT-MI). IEEE Trans Biomed Eng. 2007; 54(2):323–330. [PubMed: 17278589]
19. Xia RM, Li X, He B. Magnetoacoustic tomographic imaging of electrical impedance with magnetic induction. Appl Phys Lett. 2007; 91(8):083903.
20. Xia RM, Li X, He B. Reconstruction of Vectorial Acoustic Sources in Time-Domain Tomography. IEEE Trans Med Imaging. 2009; 28(5):669–675. [PubMed: 19211344]
21. Haacke EM, Petropoulos LS, Nilges EW, Wu DH. Extraction of conductivity and permittivity using magnetic resonance imaging. Phys Med Biol. 1991; 38(6):723–734.
22. Wen H. Noninvasive quantitative mapping of conductivity and dielectric distributions using RF wave propagation effects in high-field MRI. Proc SPIE. 2003; 5030:471–477.
23. Katscher, U.; Dorniok, T.; Findeklee, C.; Vernickel, P.; Nehrke, K. In vivo determination of electric conductivity and permittivity using a standard MR system. In: Scharfetter, H.; Merwa, R., editors. IFMBE Proc. Vol. 17. Berlin, Germany: Springer; 2007. p. 508-511.
24. Sled JG, Pike GB. Standing-wave and RF penetration artifacts caused by elliptic geometry: an electrodynamic analysis of MRI. IEEE Trans Med Imaging. 1998; 17(4):653–662. [PubMed: 9845320]
25. Alecci M, Collins CM, Smith MB, Jezzard P. Radio frequency magnetic field mapping of a 3 Tesla birdcage coil: Experimental and theoretical dependence on sample properties. Magn Reson Med. 2001; 46(2):379–385. [PubMed: 11477643]
26. Yang QX, Wang JH, Zhang XL, Collins CM, Smith MB, Liu HY, Zhu XH, Vaughan JT, Ugurbil K, Chen W. Analysis of wave behavior in lossy dielectric samples at high field. Magn Reson Med. 2002; 47(5):982–989. [PubMed: 11979578]
27. Ibrahim TS, Mitchell C, Abraham R, Schmalbrock P. In-depth study of the electromagnetics of ultrahigh-field MRI. NMR in Biomedicine. Feb; 2007 20(1):58–68. [PubMed: 17006885]
28. Akoka S, Franconi F, Seguin F, Lepape A. Radiofrequency Map of an Nmr Coil by Imaging. Magn Reson Imaging. 1993; 11(3):437–441. [PubMed: 8505878]

29. Insko EK, Bolinger L. Mapping of the Radiofrequency Field. J Mag Res Series A. Jun 1; 1993 103(1):82–85.
30. Wang JH, Qiu ML, Yang QX, Smith MB, Constable RT. Measurement and correction of transmitter and receiver induced nonuniformities in vivo. Magn Reson Med. Feb; 2005 53(2):408–417. [PubMed: 15678526]
31. Hoult DI. The principle of reciprocity in signal strength calculations - A mathematical guide. Conc Mag Res. 2000; 12(4):173–187.
32. Silvester, PP.; Ferrari, RL. Finite Element for Electrical Engineers. Cambridge: Cambridge University Press; 1996.
33. Kong, JA. Electromagnetic Wave Theory. New York: Wiley; 1986.
34. Vaughan JT, Adriany G, Snyder CJ, Tian J, Thiel T, Bolinger L, Liu H, DelaBarre L, Ugurbil K. Efficient high-frequency body coil for high-field MRI. Magn Reson Med. Oct; 2004 52(4):851–859. [PubMed: 15389967]
35. Jin, JM. Electromagnetic Analysis and Design in Magnetic Resonance Imaging. New York: CRC Press; 1999.
36. Berenger JP. A Perfectly Matched Layer for the Absorption of Electromagnetic-Waves. J Comput Phys. Oct; 1994 114(2):185–200.
37. Reza S, Vijayakumar S, Limkeman M, Huang F, Saylor C. SAR Simulation and the Effect of Mode Coupling in a Birdcage Resonator. Conc Mag Res Part B. 2007; 31B(3):133–139.
38. Haacke, EM.; Brown, PW.; Thompson, MR.; Venkatesan, R. Magnetic Resonance Imaging: Physical Principles and Sequence Design. New York: John Wiley and Sons, Inc.; 1999.
39. Schwan HP. Electrical Properties of Tissue and Cell Suspensions. Adv Biol Med Phys. 1957; 5:147–209. [PubMed: 13520431]
40. Katscher, U.; Voigt, T.; Findeklee, C. Electrical conductivity imaging using magnetic resonance tomography. Conf. Proc. Annu. Int. Conf. IEEE Eng. Med. Biol. Soc.; Minneapolis. 2009. p. 3162-3164.
41. Metzger GJ, Snyder C, Akgun C, Vaughan T, Ugurbil K, Van de Moortele PF. Local B-1(+) shimming for prostate imaging with transceiver arrays at 7T based on subject-dependent transmit phase measurements. Magn Reson Med. Feb; 2008 59(2):396–409. [PubMed: 18228604]

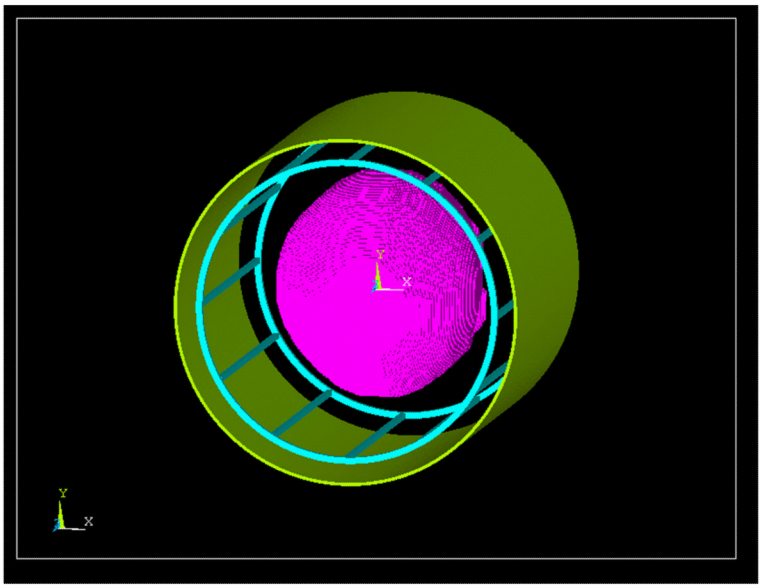

Fig. 1.
Overview of the head FEM model and a 12-rung shielded birdcage coil FEM model (green: copper shield, cyan: rungs and end-rings, magenta: head)

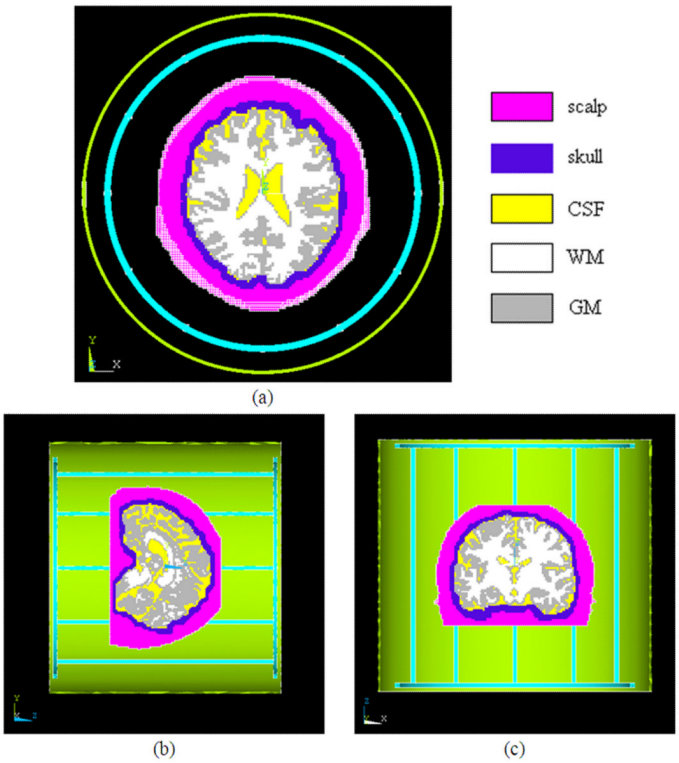

Fig. 2.
Axial (a), sagittal (b) and coronal (c) views of the FEM models. The head model was meshed with hexahedral element while the coil with tetrahedral element.

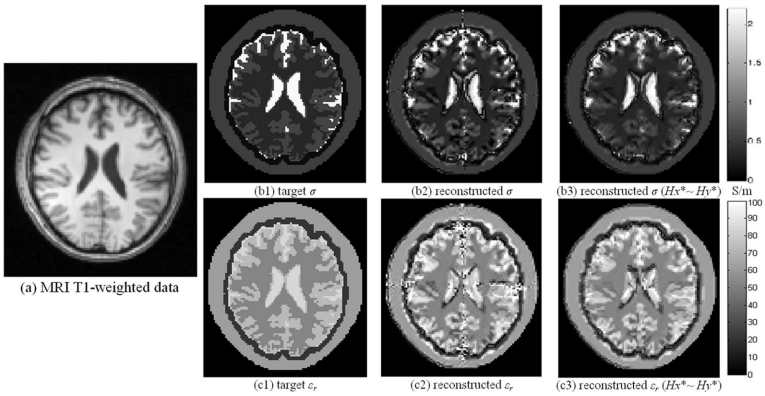

Fig. 3.

MRI T1-weighted image (a) of the slice of interest, segmented target EP distributions (b1) &. (c1), reconstructed EP distributions (b2) &. (c2), and reconstructed EP distribution (b3) &. (c3) using $H_X \sim H_Y$ data when noise free. Using the 28cm-long TEM coil, coil excitation schemes S1 and S2 were applied. Two bright stripe-like artifacts along *x*- and *y*-axes can be observed in (b2) and (c2).

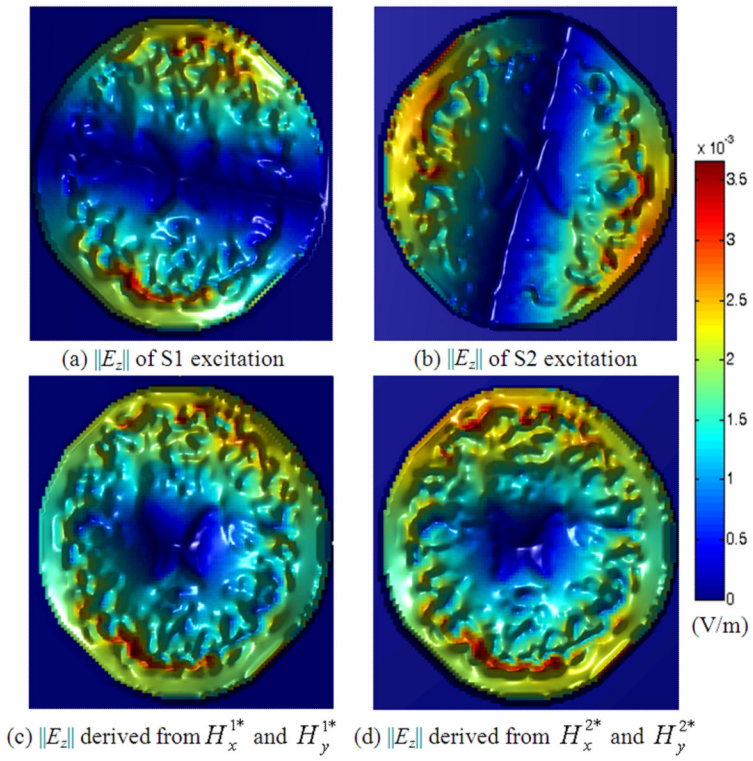

Fig. 4.

$\|E_z\|$ distribution with the TEM coil when noise-free. Coil excitation schemes S1 and S2 were applied. (a) and (b) depict $\|E_z\|$ distribution for each excitation scheme, and (c) and (d) show the $\|E_z\|$ distribution corresponding to our newly produced B_1 field. Much lower intensity can be observed along *x*- and *y*-axes in (a) and (b), and in the central area in (c) and (d).

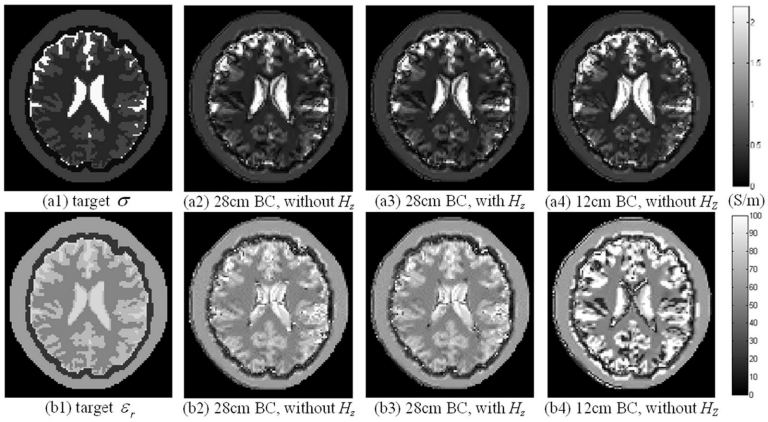

Fig. 5.

Reconstructed electric property distribution within a 28cm-long and a 12cm-long birdcage coil. Upper row: conductivity, bottom row: relative permittivity. From left to right: target EP distribution, reconstruction results without and with H_Z component in the birdcage coils, respectively.

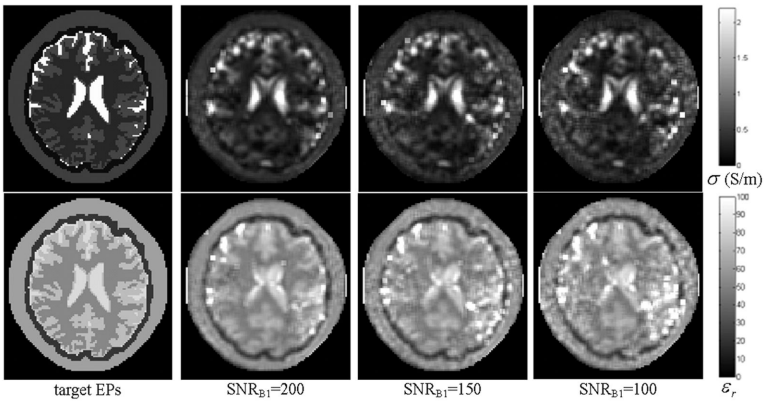

Fig. 6.

Reconstructed electric property distribution within a 28cm-long TEM coil. Upper row: conductivity, bottom row: relative permittivity. From left to right: target EP distribution, reconstruction results with decreasing SNR_{B1}.

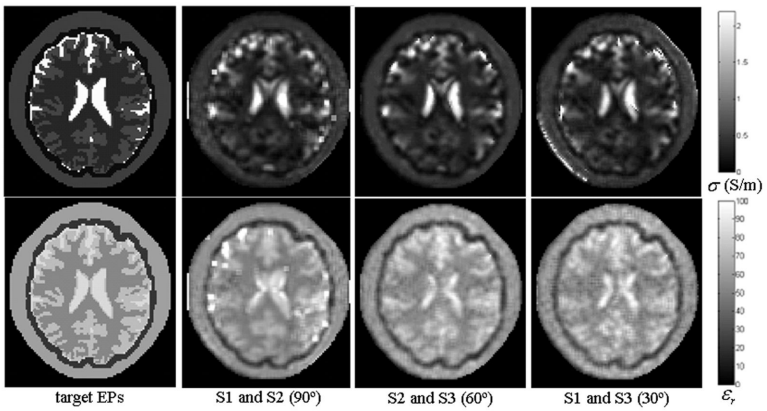

Fig. 7.

Reconstructed electric property distribution with different coil excitation scheme combinations. Upper row: conductivity, bottom row: relative permittivity. From left to right: target EP distribution and reconstructed distribution with different phase offset of the current flowing in the coil.

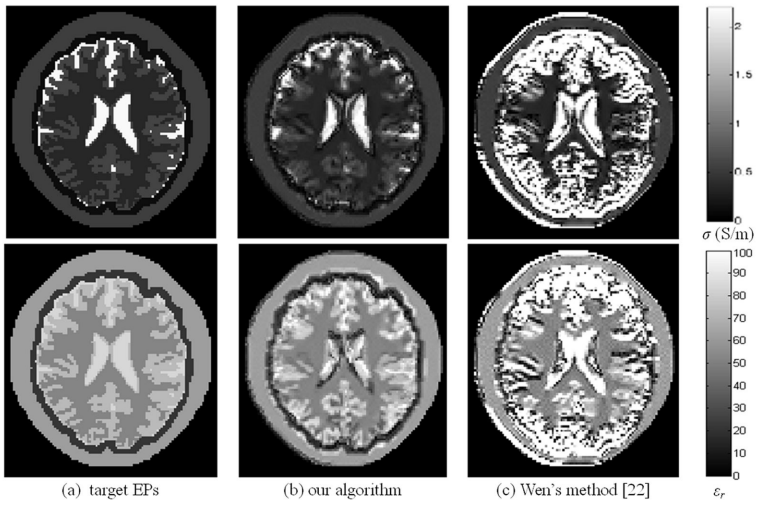

Fig. 8.

Reconstructed electric property distribution with the TEM coil when noise-free, and coil excitation schemes S1 and S2 were applied (upper row: σ distribution, bottom row: ε_r distribution; from left to right: target EPs, using our algorithm, and using Wen's method [22]).

Table I

Specifications of Coil Excitation Schemes

	current in the *i*th rung	**current feed point**	**generated magnetic field**
Scheme 1 (S1)	$I_i^{rung}=I_0\sin[(i-0.5)\pi/6]$	--	H_x^1 and H_y^1
Scheme 2 (S2)	$I_i^{rung}=I_0\sin[(i-0.5)\pi/6+\pi/2]$	90° apart from that of scheme 1	H_x^2 and H_y^2
Scheme 3 (S3)	$I_i^{rung}=I_0\sin[(i-0.5)\pi/6+\pi/6]$	30° apart from that of scheme 1	H_x^3 and H_y^3

Table II

EP Values of Head Tissues

Human head	σ (S/m)	ε_r
Scalp	0.54	62
Skull	0.12	21
CSF	2.14	84
White Matter	0.34	52
Gray Matter	0.59	73

Table III

Relative Errors and Correlation Coefficients of Reconstructed Electric Properties without and With H_Z Component Using Tem and Birdcage Coils

REs / *CCs*		28cm TEM without H_Z		28cm BC without H_Z		28cm BC with H_Z		12cm BC without H_Z	
CSF	σ	27.1%	*0.971*	30.1%	*0.899*	28.2%	*0.943*	39.4%	*0.8525*
	ε_r	24.9%	*0.936*	26.3%	*0.902*	24.3%	*0.920*	38.1%	*0.8908*
WM	σ	21.4%	*0.940*	28.6%	*0.898*	25.1%	*0.908*	38.9%	*0.8430*
	ε_r	12.7%	*0.982*	15.3%	*0.963*	12.6%	*0.987*	28.6%	*0.9258*
GM	σ	28.6%	*0.913*	32.2%	*0.888*	27.7%	*0.919*	40.6%	*0.8513*
	ε_r	18.0%	*0.969*	18.8%	*0.958*	16.5%	*0.974*	39.1%	*0.8585*

Table IV

Relative Errors and Correlation Coefficients of Reconstructed Electric Property Distribution with Decreasing SNR_{B1}.

REs / *CCs*		**SNR_{B1}=200**		**SNR_{B1}=150**		**SNR_{B1}=100**	
CSF	σ	46.4%	*0.690*	50.1%	*0.679*	67.1%	0.657
	ε_r	28.6%	*0.751*	34.4%	*0.701*	56.8%	0.659
WM	σ	39.1%	*0.788*	53.2%	*0.749*	74.4%	0.735
	ε_r	27.4%	*0.901*	33.8%	*0.874*	45.1%	0.821
GM	σ	49.1%	*0.761*	60.2%	*0.732*	74.1%	0.714
	ε_r	24.6%	*0.861*	40.9%	*0.852*	46.2%	0.811